A kinetic–hydrodynamic simulation of microstructure of liquid crystal polymers in plane shear flow

Haijun Yu, Pingwen Zhang *

CCSE, LMAM and School of Mathematical Sciences, Peking University, Beijing 100871, PR China

Abstract

We study the microstructure formation and defects dynamics arising in liquid crystalline polymers (LCPs) in plane shear flow by a kinetic–hydrodynamic coupled model. The kinetic model is an extension of the Doi theory with a non-local intermolecular potential, including translational diffusion and density variation. LCP molecules are ensured anchoring at the boundary by an additional boundary potential, meanwhile mass conservation of LCPs holds in the whole flow region. Plane Couette flow and Poiseuille flow are studied using the kinetic–hydrodynamic model and the molecular director is restricted in the shear plane. In plane Couette flow, the numerical results predict seven in-plane flow modes, including four in-plane modes reported by Rey and Tsuji [Macromol. Theory Simul. 7 (1998) 623–639] and three new complicated in-plane modes with inner defects. Furthermore, some significant scaling properties were verified, such as the thickness of the boundary layer is proportional to molecular length, the tumbling period is proportional to the inverse of shear rate. In plane Poiseuille flow, the micro-morph is quasi-periodic in time when flow viscosity and molecular elasticity are comparable. Different local states, such as flow-aligning, tumbling or wagging, arise in different flow region. The difference of the local states, or difference of the tumbling rates in near-by regions causes defects and form branch pattern in director spatial–temporal configuration figure.
© 2006 Elsevier B.V. All rights reserved.

Keywords: Nematic polymers; Microstructure; Kinetic–hydrodynamic simulation; Non-local intermolecular potential

1. Introduction

Liquid crystalline polymers (LCPs) were investigated in the last decades by several theories based on rod-like molecules [15], which include the celebrated Erickson–Leslie (LE) theory [23], the Doi kinetic theory [1] and a variety of tensor-based theories such as Hand's theory [16] for homogeneous liquid crystals (LCs), and Tsuji and Rey's phenomenological theory [28] for non-homogeneous fluid. LE theory is suitable for low molecular weight LCs and only valid for weak flow. Because of its simplicity, many numerical simulations were taken based on it. However, LE theory will become invalid near the defects where the director cannot be defined. The tensor-based theory has been applied extensively; it can describe defects and predict polydomains, which was studied by experiments [21,22]. But the earlier tensor models have a variety of parameters, and it is hard to obtain all the parameters in experiments. The most popular model in recent years is the Doi kinetic model and its extensions.

Doi developed his well-known kinetic theory for spatially homogeneous flows of rod-like LCPs, in which the excluded volume effect is accounted for by either the Onsager or the Maier–Saupe potential [1]. Later, Doi et al. extended the theory to model flows of non-homogeneous LCPs by introducing a long-range intermolecular potential [3]. Marrucci and Greco [24–26] further improved the extended Doi theory by incorporating the molecular anisotropy and the long range of interaction into the theory and approximated the non-local potential using a truncated Taylor series expansion of the probability density function (pdf) to obtain an approximate potential depending on gradients of the second moments of the pdf. Wang et al. used a more general non-local intermolecular potential taking the integral form, and obtained a closed-form stress expression accounting for the non-local molecular interaction [34]. A similar theory was developed for spheroidal LCPs by Wang et al. [35,36].

The earlier important kinetic-scale simulation based on Doi theory was carried out by Larson et al. [18,20], they expanded pdf in spherical harmonic functions to numerically solve the Doi equation with Onsager potential and predicted tumbling, wagging, log rolling, kayaking and flow-aligning. Their simulation also predicted negative first normal stress difference,

* Corresponding author. Tel.: +86 10 6275 9851; fax: +86 10 6276 7146.
  E-mail address: pzhang@pku.edu.cn (P. Zhang).

which agreed well with experiments. Later, Forest et al. gave some more detailed monodomain analysis [8–12,14,32]. For inhomogeneous flow, several simulations and analysis were carried out [2,4,7,17,29–31]. Most of them are based on closure approximation of Doi-type kinetic theory with Onsager potential, Maier–Saupe potential or Marrucci–Greco potential. As we know, closured models can reduce the computing amount a great deal, but when shear rate is very large, the orientational distortion made pdf cannot be approximated by its second moment or fourth moment, thus it may lose some features such as energy dissipation and may not arrest all monodomain attractors. The first approach of kinetic-scale simulation for inhomogeneous flow is provided by Zhou et al. [13,37]. They extended the kinetic-scale simulation of Larson to one dimensional Couette flow.

In this paper, we apply a coupled kinetic–hydrodynamic model to inhomogeneous plane shear flow. In the next section, we first introduce the kinetic–hydrodynamic model, and then the coupled model is applied to two typical plane shear LCP flow: plane Couette flow and pressure-driven Poiseuille flow. In Section 4, we present and discuss the abundant numerical results predicted by the new model. Finally, we add some concluding remarks.

2. The coupled kinetic–hydrodynamic model

2.1. Kinetic equation

The coupled kinetic–hydrodynamic model for inhomogeneous flow is a combination of an extended Doi kinetic theory for rigid rod-like molecules and the Navier–Stokes equation for incompressible flow.

The extended Doi kinetic theory includes a non-local potential,

$$U(\mathbf{x}, \mathbf{m}, t) = k_{\rm B} T \int_{\Omega} \int_{|\mathbf{m}'|=1} B(\mathbf{x}, \mathbf{m}; \mathbf{x}', \mathbf{m}') f(\mathbf{x}', \mathbf{m}', t) \, \mathrm{d}\mathbf{m}' \, \mathrm{d}\mathbf{x}', \tag{1}$$

where $f(\mathbf{x}, \mathbf{m}, t)$ is the orientational probability distribution function of LCPs, Ω the spatial region, $k_{\rm B}$ the Boltzmann constant, T the temperature and $B(\mathbf{x}, \mathbf{m}; \mathbf{x}', \mathbf{m}')$ is the interaction potential between the two polymers in the configurations $(\mathbf{x}, \mathbf{m})$ and $(\mathbf{x}', \mathbf{m}')$. If the space occupied by the polymer at position $\mathbf{x}$ with orientation $\mathbf{m}$ is denoted by $b(\mathbf{x}, \mathbf{m})$, the interaction potential function can be calculated as [1]:

$$B(\mathbf{x}, \mathbf{m}; \mathbf{x}', \mathbf{m}') = \begin{cases} U_0, & \text{if } b(\mathbf{x}', \mathbf{m}') \cap b(\mathbf{x}, \mathbf{m}) \neq \emptyset, \\ 0, & \text{otherwise.} \end{cases} \tag{2}$$

U_0 is the interaction potential constant.

The Smoluchowski equation including transitional diffusion for the LCP system is given by

$$\frac{\mathrm{d}f}{\mathrm{d}t} = \nabla \cdot \left\{ [D_{\|}\mathbf{mm} + D_{\perp}(I - \mathbf{mm})] \cdot \left(\nabla f + \frac{1}{k_{\rm B} T} f \nabla U \right) \right\}$$
$$+ D_{\rm r} \mathcal{R} \cdot \left(\mathcal{R} \cdot f + \frac{1}{k_{\rm B} T} f \mathcal{R} U \right) - \mathcal{R} \cdot (\mathbf{m} \times \kappa \cdot \mathbf{m} f), \tag{3}$$

where $D_{\rm r} = k_{\rm B} T / \xi_{\rm r}$, $\xi_{\rm r} = 1/3\pi\eta_{\rm s} l^3 / (\ln(l/b) - c)$, $D_{\|} = 1/6 D_{\rm r} l^2$, $D_{\perp} = 1/12 D_{\rm r} l^2$, $\eta_{\rm s}$ the coefficient of solvent viscosity, $\xi_{\rm r}$ the rotational friction factor and $c = 0.8$ is a dimensionless constant. $D_{\|}$, $D_{\perp}$, $D_{\rm r}$ are the translational diffusion coefficients parallel and normal to the orientation and rotational diffusion of the LCP molecules [1], ∇ the gradient operator with respect to the variable $\mathbf{x}$, $\mathcal{R} = \mathbf{m} \times (\partial/\partial\mathbf{m})$ is the rotational gradient operator, $\kappa = (\nabla\mathbf{v})^{\rm T}$ is the velocity gradient tensor, and d/dt is the material derivative $(\partial/\partial t) + \mathbf{v} \cdot \nabla$.

2.2. Hydrodynamic equations

For simplicity, we neglect the density variation in terms of concentration variation in LCP solution. Then the macroscopic system consists of the continuity equation with form:

$$\nabla \cdot \mathbf{v} = 0, \tag{4}$$

and momentum equation:

$$\rho \frac{\mathrm{d}\mathbf{v}}{\mathrm{d}t} + \nabla p = \eta_{\rm s} \Delta \mathbf{v} + \nabla \cdot \tau_p + \mathbf{F}^e, \tag{5}$$

where $\mathbf{F}^e = -\langle \nabla U \rangle$ is the body force induced by the long-range molecular interaction [34], p the static pressure and τ_p is the LCP viscoelastic stress:

$$\tau_p = 2k_{\rm B} T \nu \xi_{\rm r} D : \langle \mathbf{mmmm} \rangle - \left\langle \mathbf{mm} \times \left(k_{\rm B} T \frac{\mathcal{R} f}{f} + \mathcal{R} U \right) \right\rangle. \tag{6}$$

Here, $\mathbf{D} = (\kappa + \kappa^{\rm T})/2$, and

$$\langle(\cdot)\rangle = \int_{|\mathbf{m}|=1} (\cdot) f(\mathbf{m}, \mathbf{x}, t) \, \mathrm{d}\mathbf{m}. \tag{7}$$

The first term of (6) is the viscous stress from solvent–LCP interaction and the second term is the elastic stress. For more details see [34].

2.3. Dimensionless equations

Let L_0 denote the characteristic scale of the flow region, ℓ the length of LCP molecules, and V_0 the characteristic velocity of the flow. The kinetic equation and hydrodynamic equation have different spatial and temporal scales. We rescale the system using the flow region size L_0, the flow time $T_0 = L_0/V_0$ and the Boltzmann constant multiplied by the temperature:

$$\mathbf{x}^* = \frac{\mathbf{x}}{L_0}, \qquad t^* = \frac{t}{T_0}, \qquad \mathbf{v}^* = \frac{\mathbf{v}}{V_0}, \qquad U^* = \frac{U}{k_{\rm B} T},$$

and rewrite $\mathbf{x}^*, t^*, \mathbf{v}^*, U^*$ as $\mathbf{x}, t, \mathbf{v}, U$. Then the non-dimensional form of the kinetic–hydrodynamic system becomes:

$$\frac{\partial f}{\partial t} + \nabla \cdot (\mathbf{v}f) = \frac{\varepsilon^2}{De} \nabla \cdot \{[D_{\perp}^*(\mathbf{I} + \mathbf{mm})] \cdot (\nabla f + f \nabla U)\}$$
$$+ \frac{1}{De} \mathcal{R} \cdot (\mathcal{R}f + f\mathcal{R}U) - \mathcal{R}(\mathbf{m} \times \kappa \cdot \mathbf{m}f), \tag{8}$$

$$\frac{\partial \mathbf{v}}{\partial t} + (\mathbf{v} \cdot \nabla)\mathbf{v} + \nabla p = \frac{1 - \gamma}{Re} \Delta \mathbf{v} + \frac{\gamma}{ReDe}(\nabla \cdot \tau^p + \mathbf{F}^e), \tag{9}$$

$$\tau_{\alpha\beta}^{(p)} = 3S_{\alpha,\beta} - \langle (m \times \mathcal{R}U)_\alpha m_\beta \rangle + \frac{De}{2}\kappa_{kl}\langle m_\alpha m_\beta m_k m_l \rangle,$$

$$S_{i,j} = \left\langle m_i m_j - \frac{1}{3}\delta_{ij} \right\rangle, \tag{10}$$

where

$$De = \frac{V_0/L_0}{D_r}, \qquad \varepsilon = \frac{\ell}{L_0}, \qquad Re = \rho\frac{V_0 L_0}{\eta_s + \nu\xi_r},$$

$$\gamma = \frac{\nu\xi_r}{\eta_s + \nu\xi_r}, \qquad D_\perp^* = \frac{\ln(\ell/b)}{12(\ln \ell/b) - c)}.$$

2.4. Anchoring condition

Proper boundary conditions should be given before solving the system (4), (8), (9). The boundary condition for macroscopic hydrodynamic equation is standard. But the boundary condition of the Smoluchowski equation should be delicately picked.

Chemists can make the boundary molecules anchor at given angle by milling the container's surface, which yields the well-known **anchoring condition**. The director of the boundary molecules is fixed, but the number density is not fixed. So we cannot just give a fixed value to pdf $f(\mathbf{x}, \mathbf{m}, t)$ on boundary. Furthermore, the conservation of the molecules yields that $\int_\Omega \int_{|\mathbf{m}|=1} f(\mathbf{x}, \mathbf{m}, t)\,d\mathbf{m}\,d\mathbf{x}$ should be constant. Taking into account all aspects of the case, we add a boundary potential accounting for interaction between polymers and molecules of boundary surfaces to the system, instead of giving a fixed value to the pdf at the boundary:

$$\tilde{U}(\mathbf{x}, \mathbf{m}, t) = k_B T \int_{\partial\Omega} \int_{|\mathbf{m}|=1} \tilde{B}(\mathbf{x}, \mathbf{m}; \mathbf{x}', \mathbf{m}')\tilde{f}(\mathbf{x}', \mathbf{m}', t)\,d\mathbf{m}'\,d\mathbf{x}', \tag{11}$$

where $\tilde{f}(\mathbf{x}', \mathbf{m}', t)$ is the pdf of boundary molecules anchoring at the boundary surface. $\tilde{B}(\mathbf{x}, \mathbf{m}; \mathbf{x}', \mathbf{m}')$ is the interaction potential function between LCP molecules and boundary molecules. Assume that the pdf of boundary molecules is the Dirac function. Then

$$\tilde{U}(\mathbf{x}, \mathbf{m}, t) = k_B T \tilde{N} \int_{\partial\Omega} \int_{|\mathbf{m}'|=1} \tilde{B}(\mathbf{x}, \mathbf{m}; \mathbf{x}', \mathbf{m}')\delta(\mathbf{m}' - \mathbf{m}_0(t))$$

$$\times d\mathbf{m}'\,d\mathbf{x}' = k_B T \tilde{N} \int_{\partial\Omega} \tilde{B}(\mathbf{x}, \mathbf{m}; \mathbf{x}'; \mathbf{m}_o(t))\,d\mathbf{x}'. \tag{12}$$

We replace the potential $U(\mathbf{x}, \mathbf{m}, t)$ in the Smoluchowski equation by

$$U^t = U + \tilde{U}.$$

Integrating the both side of the Smoluchowski equation, and noticing that the pdf $f(\mathbf{x}, \mathbf{m}, t)$ is periodic with respect to $\mathbf{m}$, one
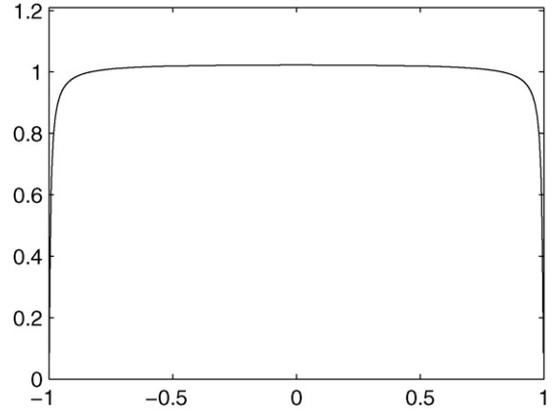

Fig. 1. Function $g_\alpha(x)$ with $\alpha = 0.01$.

obtains:

$$\frac{d}{dt} \int_\Omega \int_{|m|=1} f\,d\mathbf{m}\,d\mathbf{x} = \frac{\varepsilon^2}{De} \int_{|\mathbf{m}|=1} \int_{\partial\Omega}$$

$$\{[D_\| \mathbf{mm} + D_\perp(\mathbf{I} - \mathbf{mm})] \cdot (\nabla f + f\nabla U^t)\} \cdot \mathbf{n}\,d\mathbf{x}\,d\mathbf{m}. \tag{13}$$

We take the boundary condition of the Smoluchowski equation as follows:

$$\{[D_\| \mathbf{mm} + D_\perp(\mathbf{I} - \mathbf{mm})] \cdot (\nabla f + f\nabla U^t)\} \cdot \mathbf{n} = 0, \quad \mathbf{x} \in \partial\Omega. \tag{14}$$

3. Application to plane shear flow

We assume the flow direction is along x-axis, shearing along y, and the LCP molecules lying in the xy plane. Let θ be the angle between $\mathbf{m}$ and the x-axis. Let C denote the driven pressure, and assume the system is homogeneous in x direction. Then

$$\mathbf{x} = (x, y)^T, \qquad \mathbf{v} = (u, v)^T, \qquad \mathbf{m} = (\cos\theta, \sin\theta)^T,$$

$$\nabla = (0, \partial y)^T, \qquad \nabla p = (C, p_y)^T, \qquad \kappa = \begin{pmatrix} 0 & u_y \\ 0 & 0 \end{pmatrix}.$$

$b(\mathbf{x}, \mathbf{m}) = b(x, y, \theta)$ is a $\ell \times b$ rectangle at position (x, y). $B(\mathbf{x}, \mathbf{m}; \mathbf{x}', \mathbf{m}')$ defined by: (2) takes the form $B(x, y, \theta; x', y', \theta')$. It can be calculated by

$$U_0 G\left(\frac{(x' - x)\cos\theta + (y' - y)\sin\theta}{\ell + \ell\cos(\theta' - \theta)/2}\right)$$

$$\times G\left(\frac{(x' - x)\sin\theta - (y' - y)\cos\theta}{(\ell\sin(\theta' - \theta) + b)/2}\right), \tag{15}$$

where $G(x)$ is the characteristic function of the region $[-1, 1]$; it can be approximated by (see Fig. 1)

$$g_\alpha(x) = \frac{2}{\int_{-1}^1 \exp(\alpha/x^2 - 1)\,dx} \exp\left(\frac{\alpha}{x^2 - 1}\right). \tag{16}$$

We use the following formula to approximate (15):

$$B(x, y, \theta; x', y', \theta') = N \sin^2(\theta' - \theta)$$

$$\times g_\alpha \left(\frac{(x' - x) \cos \theta + (y' - y) \sin \theta}{\ell} \right)$$

$$\times g_\alpha \left(\frac{(x' - x) \sin \theta - (y' - y) \cos \theta}{\ell/2} \right), \quad (17)$$

where $N = U_0/4$. We note that the excluded volume potential determined by (17) can deduce the Marrucci–Greco potential, and it becomes the Maier–Saupe potential when α goes to 0.

The dimensionless Smoluchowski equation including the boundary potential can be written as:

$$\frac{\partial f}{\partial t} = \frac{\varepsilon^2}{De} \partial_y[(D_\perp(1 + \cos^2 \theta)(f_y + fU_y^t)] + \frac{1}{De} \partial_\theta(f_\theta + fU_\theta^t)$$

$$+ \partial_\theta(fu_y \sin^2 \theta), \quad (y, \theta) \in [0, 1] \times [0, 2\pi], \quad (18)$$

$$U^t = U + \tilde{U}, \quad (19)$$

$$U(y, \theta, t) = N \int_0^{2\pi} \int_{-1}^1 K(y' - y, \theta) \sin^2(\theta' - \theta) f(y', \theta', t)$$

$$\times dy' \, d\theta', \quad (20)$$

$$\tilde{U}(y, \theta, t) = \tilde{N} \frac{2}{\ell} \left(g_\alpha \left(\frac{y - 0}{\ell/2} \right) + g_\alpha \left(\frac{y - 1}{\ell/2} \right) \right) \sin^2(\theta - \theta_b(t)), \quad (21)$$

where

$$K(y, \theta) = \int_{-1}^1 \frac{2}{\ell^2} g_\alpha \left(\frac{x \cos \theta + y \sin \theta}{\ell/2} \right)$$

$$\times g_\alpha \left(\frac{x \sin \theta - y \cos \theta}{\ell/2} \right) dx. \quad (22)$$

The momentum equation for plane shear flow is:

$$u_t + C = \frac{1 - \gamma}{Re} u_{yy} + \frac{\gamma}{ReDe} \partial_y \tau_{21}, \quad y \in [0, 1]. \quad (23)$$

$$\tau_{21} = 2\langle \sin \theta \cos \theta \rangle + (U_\theta \cos^2 \theta) + \frac{De}{2} u_y \langle \sin^2 \theta \cos^2 \theta \rangle, \quad (24)$$

where C is the dimensionless driven pressure gradient, and we have $C = 0$, $u(0) = 0$, $u(1) = 1$, for plane Couette flow; $C = -4(1 - \gamma)/Re$, $u(0) = u(1) = 0$, for pressure-driven plane Poiseuille flow (Fig. 2).

3.1. Numerical scheme and choice of parameters

The model includes seven parameters: Deborah number De, the ratio of molecular length to the size of the flow region ε, dimensionless translational diffusion coefficient normal to the
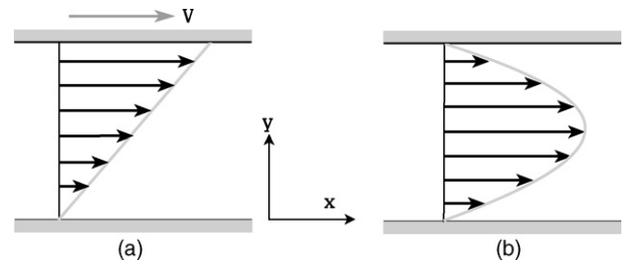

Fig. 2. The plane shear flow of Newtonian fluid: (a) Couette flow, no pressure gradient, upper plate moving; (b) Poiseuille flow, pressure gradient $\partial p/\partial x$ with both plates fixed.
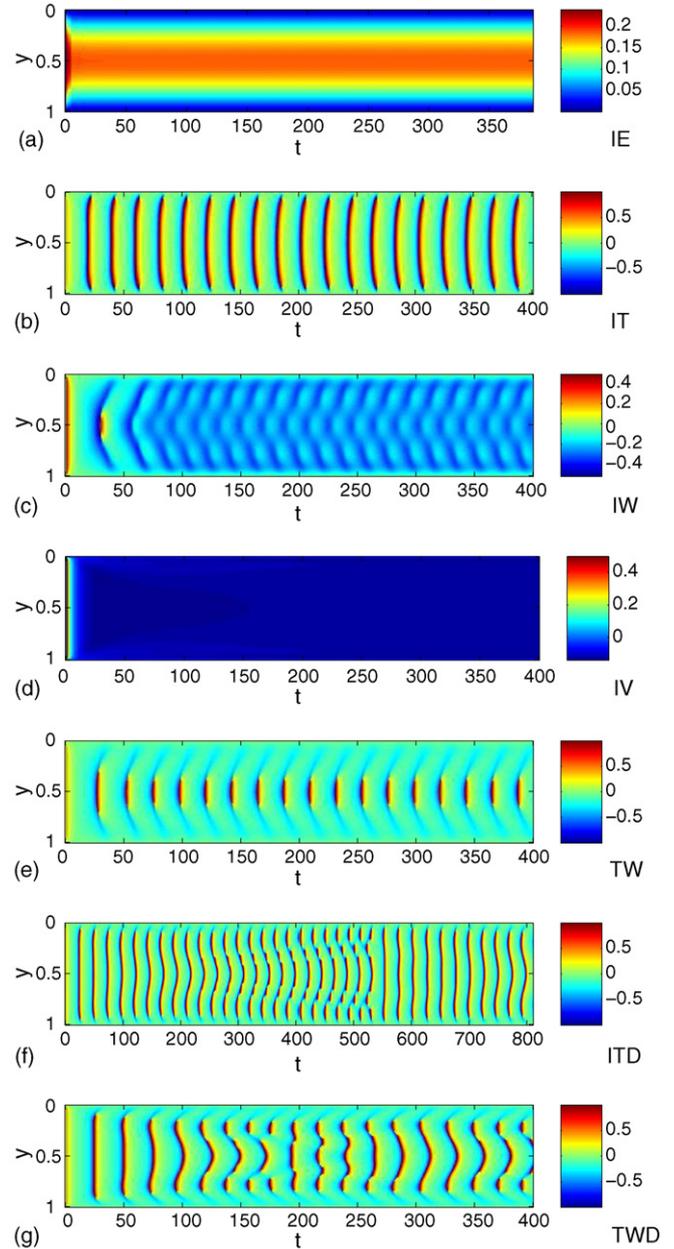

Fig. 3. The director configurations of seven phases. Colors represent the director angle's sine value (from −1 to 1). The horizontal axis is dimensionless time and the vertical axis is the distance to lower slab. The parameters are $D_\perp = 0.1$, $\gamma = 0.1$, $Re = 1$, $N = 5$. (a) $\varepsilon = 0.02$, $De = 0.005$; (b) $\varepsilon = 0.02$, $De = 0.1$; (c) $\varepsilon = 0.05$, $De = 0.75$; (d) $\varepsilon = 0.05$, $De = 1$; (e) $\varepsilon = 0.05$, $De = 0.7$; (f) $\varepsilon = 0.02$, $De = 0.4$; (g) $\varepsilon = 0.02$, $De = 0.7$.

Table 1
Thickness of the boundary layer, $N = 5$, $D_\perp = 0.1$, $Re = 1$, $\gamma = 0.1$

De	ε			
	0.1	0.05	0.02	0.01
0.1	FA	0.170	0.060	0.031
0.2	0.240	0.140	0.055	0.028

Table 2
Thickness of the boundary layer, $N = 10$, $D_\perp = 0.1$, $Re = 1$, $\gamma = 0.1$

De	ε			
	0.1	0.05	0.02	0.01
0.1	FA	0.195	0.075	0.040
0.2	0.250	0.158	0.060	0.030
0.5	0.190	0.108	0.040	0.020
1	0.140	0.078	0.030	0.015
2	0.090	0.050	0.020	0.009

molecular orientation $D_\perp$, the proportion of polymer viscosity to total viscosity γ, the coefficient of the excluded volume potential N, the strength of the additional boundary potential $\tilde{N}$ and Reynolds number Re. To focus on LCP behavior dependence on De, ε, we specify $Re = 1$ to get laminar flow; $D_\perp = 0.1$
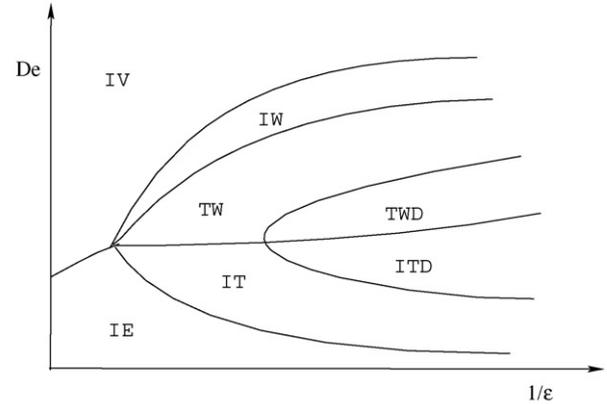

Fig. 4. Rheological phase diagram as a function of the ratio of micro to macro spatial scale $1/\varepsilon$ and the ratio of micro to macro time scale De (at $D_\perp = 0.1$, $\gamma = 0.1$, $Re = 1$, $N = 5$).

for $l/b \approx 120$; $N = 5$ to ensure nematic phase; $\gamma = 0.1$ for dilute solution; and $\tilde{N}$ has the right magnitude to ensure boundary anchoring.

Eqs. (18)–(24) were solved numerically using a finite-difference scheme. A second-order difference scheme was used in y and θ direction, and the fourth-order Runge–Kutta method for time-stepping. The no-slip boundary condition was used for
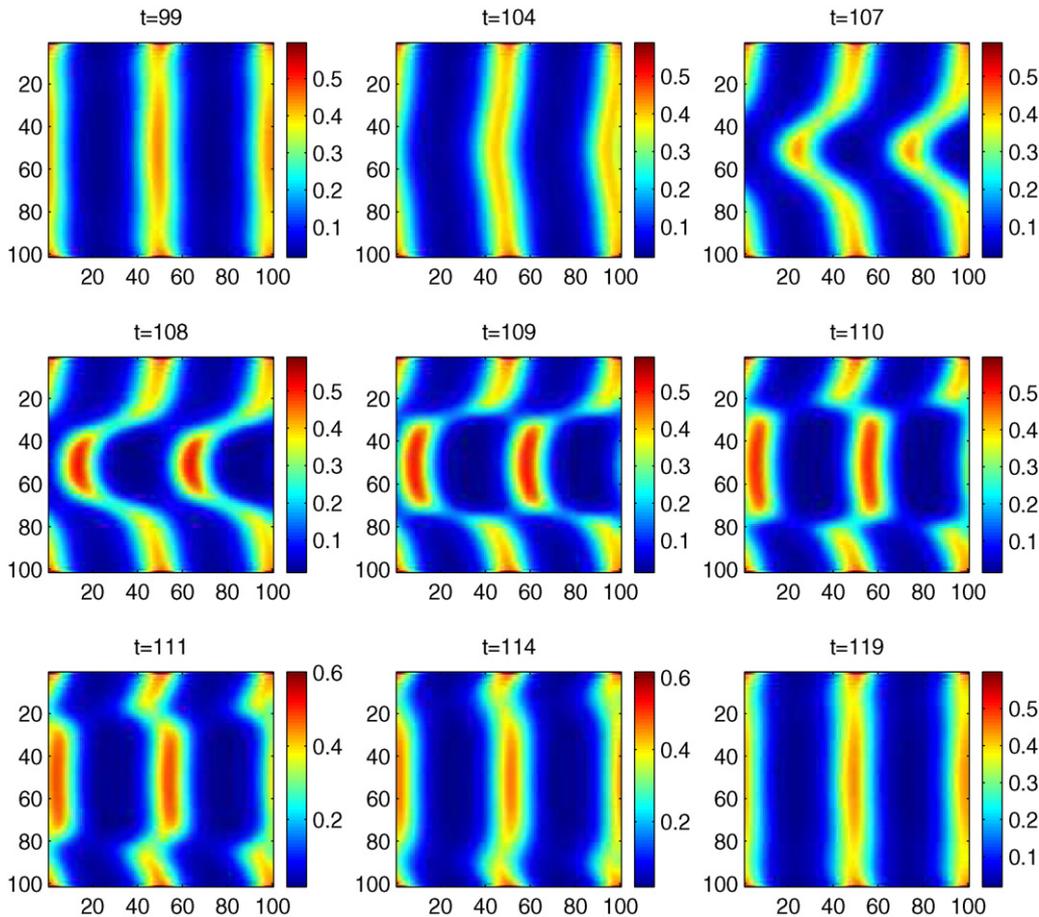

Fig. 5. Demonstration of pdf in one tumbling period at $N = 5$, $De = 0.5$, $\varepsilon = 0.05$. The x-axis is θ, 0–100 in the figure means from $-\pi$ to π. The y-axis is y, 0–100 in the figure means from 0 to 1. From left to right, top to bottom the dimensionless time is: 99, 104, 107, 108, 109, 110, 111, 114, 119. Strong defects arise at time $t = 109$ (the middle figure) at about $y = 0.28, 0.72$.

Table 3
Flow-aligning angle at $y = 0.5$ when $N = 5$, $D_\perp = 0.1$, $Re = 1$, $\gamma = 0.1$, $\varepsilon = 0.05$

θ_b	De							
	1	4	16	64	256	1024	4096	16384
0	−0.0599	0.0347	0.0841	0.0787	0.0574	0.0376	0.0238	0.0149
$\pi/2$	−0.1057	0.0313	0.0838	0.0787	0.0574	0.0376	0.0238	0.0149

the momentum equation. We verified that pdf f is positive and its integral keeps constant in the numerical process.

To resolve the microstructure, the cell size in y direction should be smaller than ε, 400×100, 200×100, $100 \times 100, 100 \times 100$ grids are used for $\varepsilon = 0.01, 0.02, 0.05, 0.1$. We refined the grid, but that did not make much difference.

In the numerical results, close attention should be paid to the following quantities: density $\rho = \langle 1 \rangle$; the order of nematic $s = \sqrt{\langle \cos 2\theta \rangle^2 + \langle \sin 2\theta \rangle^2}/\rho$; the angle between director and flow direction $\phi = \arcsin(\langle \sin 2\theta \rangle / \sqrt{2s^2 + 2s \langle \cos 2\theta \rangle})$; the derivative of stress at y direction τ_y, and so on.

4. Results and discussion

4.1. Plane Couette flow

We first simulated the case $N = 5$, $\varepsilon = 0.02$, $De = 0.5$, $D_\perp = 0.1$, $\gamma = 0.1$, $Re = 1$, then varied the parameters separately. We found that the microstructure is mainly determined by N, ε, De, and is not sensitive to other parameters, except that the feedback of microstructure to the velocity field has strong relation with γ.

4.1.1. Flow modes

In the case of plane Couette flow, the coupled model predicts not only all in-plane phases reported by Rey and Tsuji [29], but also three new phases. The four in-plane phases both predicted by Tsuji and Rey's phenomenological theory and our kinetic–hydrodynamic model are:

- *In-plane elastic-driven steady state* (IE): Steady state arises due to the long-range order elasticity stored in the spacial deformed pdf field. In this mode there is no orientation boundary layer because of no flow-alignment in the bulk region. See Fig. 3(a).
- *Tumbling state* (IT): In this time-dependent mode, the director in the bulk region is rotational (tumbling), and in the boundary is oscillatory or flow-aligning. The boundary between the bulk tumbling region and each boundary layer is characterized by the periodic emergence of the abnormal nematic phase, in which the director is not defined, called defect. Defects link the tumbling region and fixed director region like bearings. See Fig. 3(b).
- *In-plane wagging state* (IW): In this mode, the director dynamics over the entire flow geometry is wagging with an amplitude that decreases from a maximum at the centerline to the two boundary surfaces when ε is relatively big, but when ε is very small, there will be a bulk wagging region with the same amplitude and two boundary layers with amplitude decreasing to zero. See Fig. 3(c).

- *Viscous-driven steady state* (IV): In this mode, the flow phase in the inner bulk region is flow-aligning and the anchoring angle is very close to zero. There will be two boundary layers if the boundary anchoring angle is different from the bulk flow-aligning angle. See Fig. 3(d).

Beyond that, the kinetic–hydrodynamic model predicts three new flow modes:

- *Tumbling–wagging composite region* (TW): In this time-dependent mode, there is no boundary layer; instead, a wide wagging region arises between two anchoring boundary surfaces and the tumbling region in the middle of the flow. One may take this mode as turning from IT mode to IW mode. See Fig. 3(e).
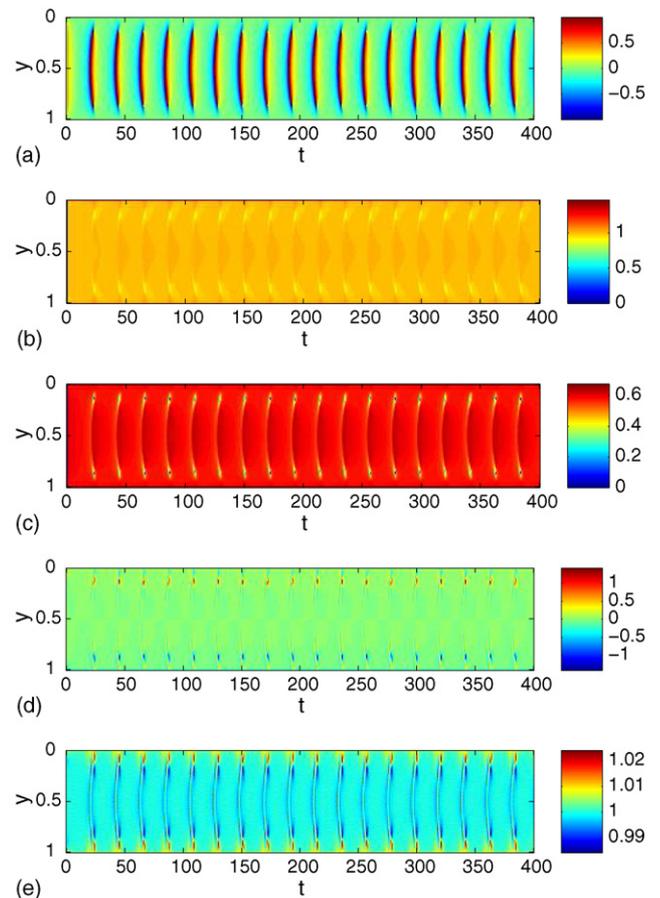

(a)

(b)

(c)

(d)

(e)

Fig. 6. The effects of defects $N = 5$, $\varepsilon = 0.05$, $De = 0.2$, $\theta_b = 0$. The x-axis is dimensionless time. The y-axis is spatial position. (a) The sine value of angle between director and flow direction $\mathbf{n}$; (b) density ρ; (c) order parameter s; (d) the derivative of stress at y direction τ_y; (e) shear rate u_y.
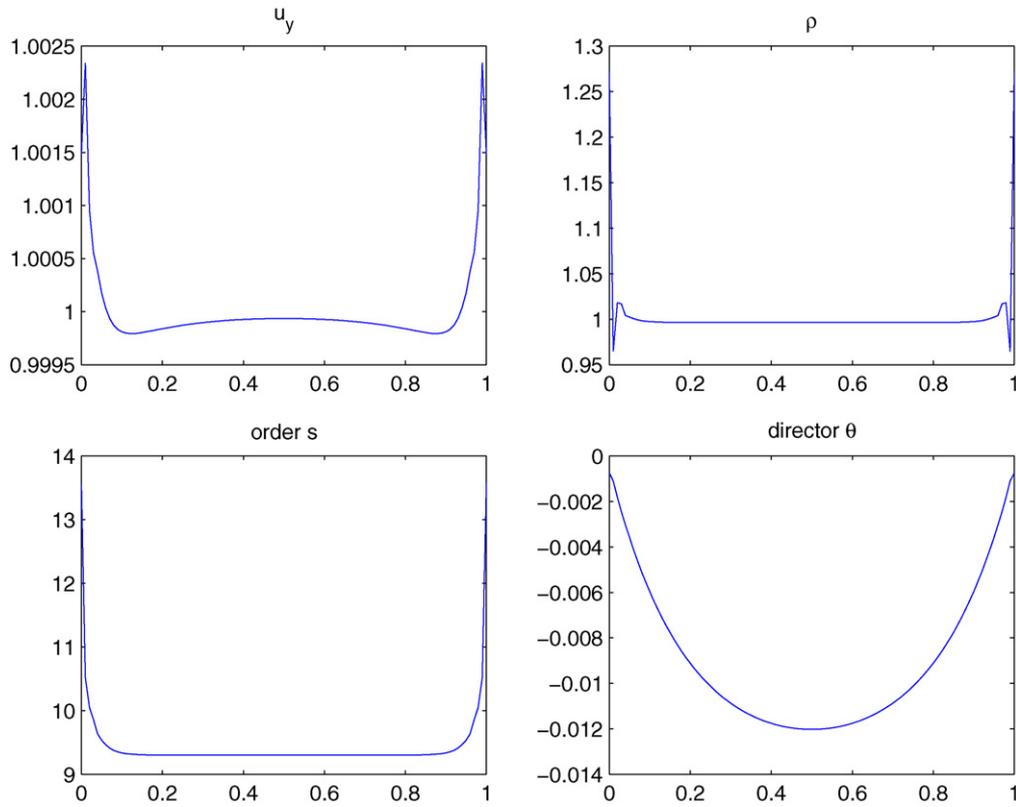
Fig. 7. Weak flow results at $N = 5$, $\varepsilon = 0.05$, $De = 0.01$, $\theta_b = 0$. The x-axis is spatial position and the y-axis is the value of the plot function. There are fluctuations near the two boundaries in shear rate u_y and density ρ, this is one of the effects of the boundary potential. Another effect is that the order function s gets its maximum on the two boundaries.

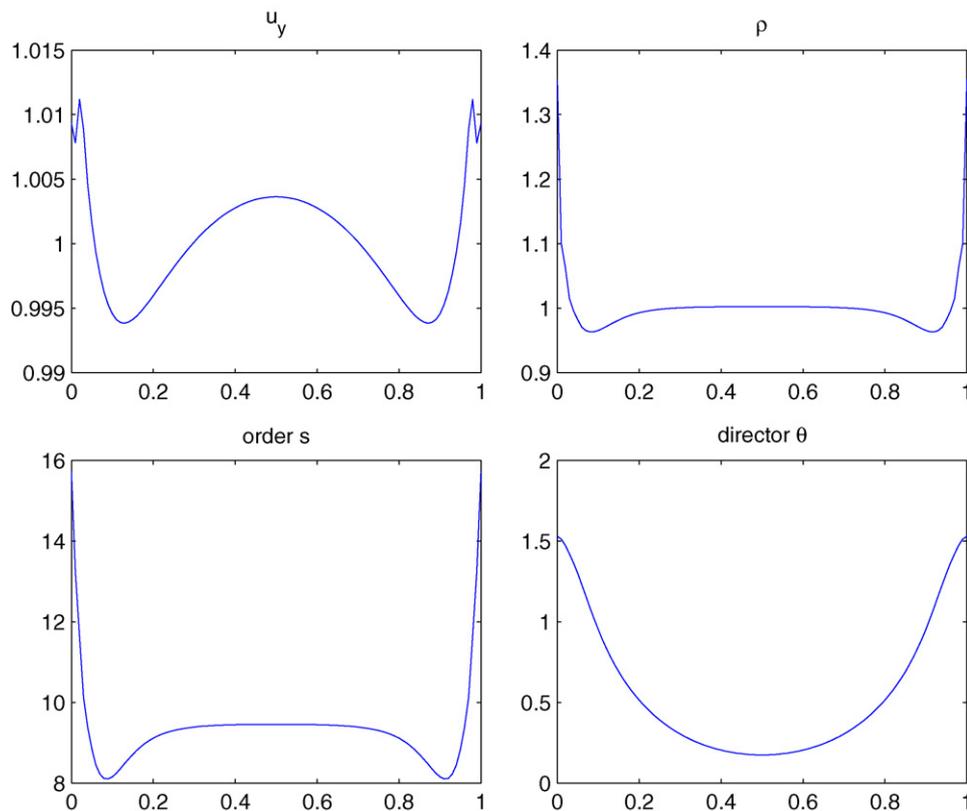Fig. 8. Weak flow results at $N = 5$, $\varepsilon = 0.05$, $De = 0.01$, $\theta_b = \pi/2$. The x-axis is spatial position and the y-axis is the value of the plot function.
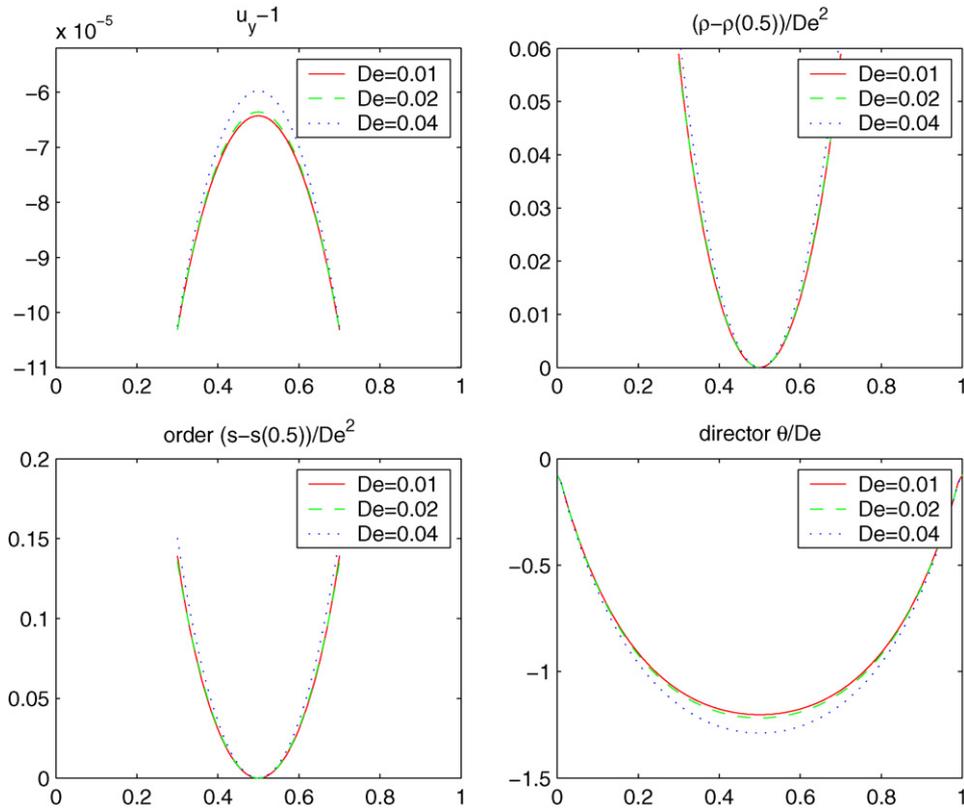
Fig. 9. Scaling properties when $N = 5$, $\varepsilon = 0.05$, $De = 0.01$, 0.02, 0.04, $\theta_b = 0$. From left to right, top to bottom, the figures show shear rate, density, order parameter and director angle. The x-axis is spatial position and the y-axis is the value of the plot function. These results confirm the scaling property found by Forest et al., except for two boundary layers for shear rate, density and order parameter, which was affected heavily by the boundary potential.
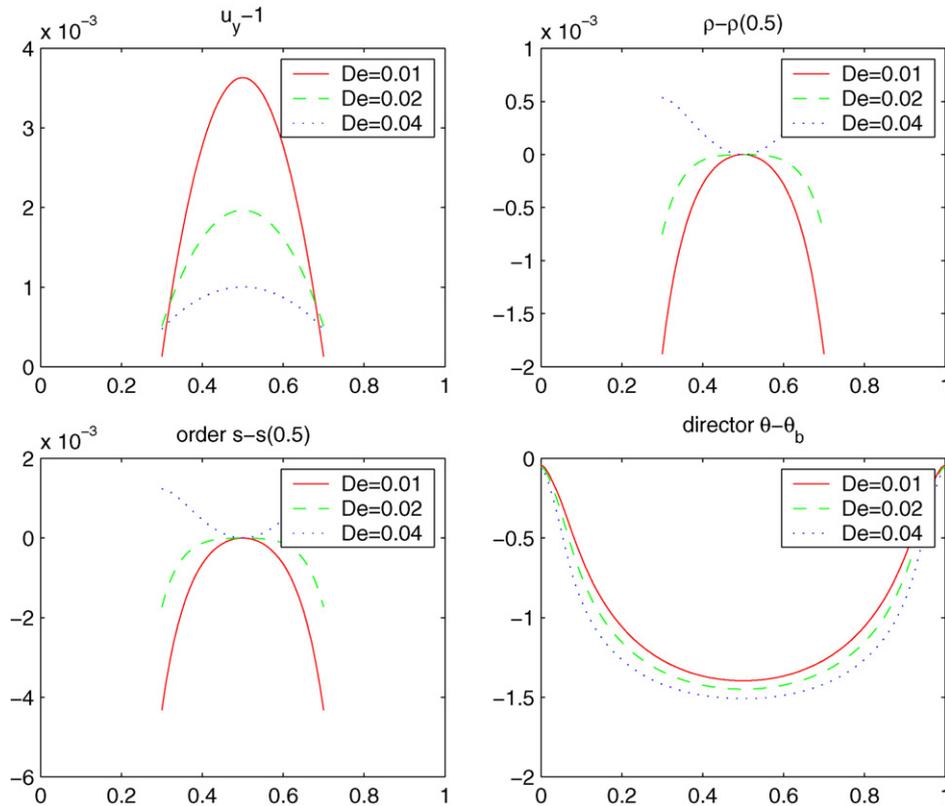

Fig. 10. Scaling properties when $N = 5$, $\varepsilon = 0.05$, $De = 0.01$, 0.02, 0.04, $\theta_b = \pi/2$. From left to right, top to bottom, the figures show shear rate, density, order parameter and director angle. The x-axis is spatial position and y-axis is the value of the plot function. We did not get the scaling properties found by Forest et al. even in the inner bulk region.

- *Tumbling state with inside defects* (*ITD*): This is a quasi-periodic mode. In general, the director is tumbling in the bulk region but the tumbling rate does not fit together well. This disharmony introduces inside defects. See Fig. 3(f).
- *Tumbling–wagging composite region with inside defects* (*TWD*): In this quasi-periodic mode, a wide wagging region arises between the middle bulk tumbling region with inside defects and two anchoring boundary surfaces. See Fig. 3(g).

We think the inner defects arise because of the decaying of long-range elasticity as the ratio of molecular length to the gap of the plates ε tends to zero, so the effects of the defects near the boundaries can easily spread into the inner bulk region and give rise to out-of-step of the tumbling rate then trigger inner defects. To make sure the three new modes are introduced by translational diffusion, we also carry out many simulations without translational diffusion. We do not find modes with inner defects in the corresponding ε, De region.

Fig. 4 is a schematic of the rheological phase diagram given in terms of De and $1/\varepsilon$. For big ε, there are only two flow modes IE and IV, since the flow region has the same scale as molecular scale. In fact, we tried several parameters, but obtained no IT phase when $\varepsilon = 0.2$. For a middle ε, the director configure shows IE, IT, TW, IW, IV as De changing from a very small value to a sufficiently big value. When ε is small enough, the long-range elasticity becomes very small, so more defects will arise to balance the viscosity, which leads to ITD and TWD phase. In ITD and TWD flow mode, the director configure shows multilayer structure of defects.

Note that the phase diagram depends heavily on the molecular interaction strength N. With increasing N, the amount of inside defects decreases.

4.1.2. Thickness of the boundary layer d

The scaling property of the thickness of the boundary layer predicted by the coupled model is $d \propto \varepsilon$, see Table 1. This is compatible with Marrucci Scaling $Er^{-1/2}$, because $Er \propto 1/\varepsilon^2$ in the coupled model. When the boundary anchoring angle is changed, for example from 0 to $\pi/2$, the microstructure does not change in essence, the only change is the enlarging of the boundary layer. The thickness of the boundary layer when the anchoring angle is $\pi/2$ is about twice as large as when the anchoring angle is zero degree. When N increases, the thickness of the boundary layer increases more slowly at lower De number. It is more sensitive to the De number than to N. See Tables 1 and 2.

4.1.3. Tumbling rate and flow-aligning angle

The director rotates in a clockwise direction ($\dot{\phi} < 0$) in the tumbling state; see Figs. 4 and 5. The tumbling period almost does not depend on the dimensionless parameter De, ε when it is far away from phase transition points. When $N = 5$, there are about 20 tumbling periods in dimensionless time $t = 400$. Because time is rescaled by $T_0 = L_0/V_0 = 1/\dot{\gamma}$ so $T \propto 1/\dot{\gamma}$. If N increases, the tumbling period becomes shorter. The scaling property is about $T \propto 1/N$. The tumbling rate $\dot{\phi}(\phi)$ is not constant [27]: it attains the minimum when $\phi \approx \phi_{FA}$, and attains the maximum when ($\phi \approx \phi_{FA} \pm \pi/2$, ϕ_{FA} is the flow-aligning angle.

When De approaches infinity, ϕ_{FA} tends to zero, but slowly; see Table 3.

4.1.4. The effects of defects

The defects take an important role in the microstructure dynamics. When spatial distortion is not tremendous, the LCPs in the flow region will take a local state, tumbling, wagging or flow-aligning, according to the local dimensionless parameters De, N. If the tumbling rates of neighboring LCPs are different, or tumbling region is connected with wagging or flow-aligning, the defects will arise. Defects connect tumbling regions with other phases like a bearing.

LCPs are in abnormal nematic phase where defects arise, the order parameter is about zero. The minimum of the excluded volume potential is bigger than that in the normal nematic state. This causes lower density in defect core, see Fig. 6(b). Defects also introduce big stress variation, see Fig. 6(d). The big stress variation causes the shear rate to become larger that is we have shear thinning; see Fig. 6(e).

4.1.5. Weak shear results

Forest et al. studied a weak shear tensor model by asymptotic analysis [14], and obtained $s = s_0 + De^2 s_2 + O(De^3)$,
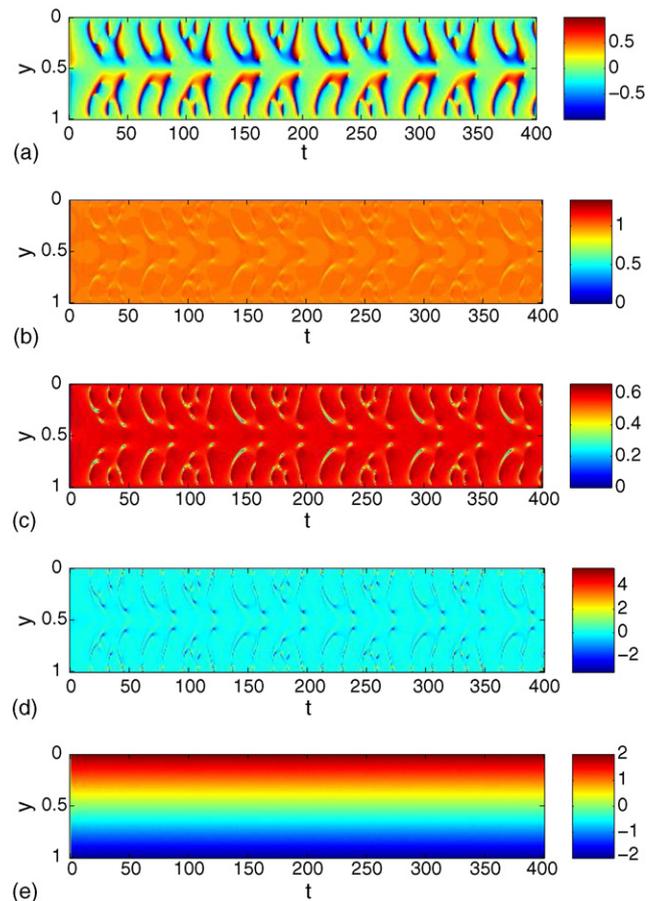

Fig. 11. Figures demonstration of typical pressure-driven plane Poiseuille flow, $N = 5$, $\varepsilon = 0.02$, $De = 0.2$, $\theta_b = 0$. (a) The sine value of angle between director and flow direction $\sin \phi$; (b) density ρ; (c) order parameter s; (d) the derivative of stress at y direction τ_y; (e) shear rate u_y.
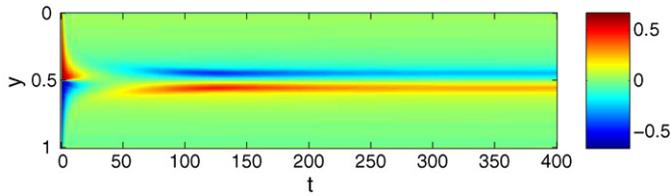
Fig. 12. Director angle's spatial–temporal configuration of flow-aligning mode in pressure-driven plane Poiseuille flow, $N = 5$, $\varepsilon = 0.02$, $De = 2$.

$\phi = \phi_0 + De\phi_1 + O(De^2)$, when the anchoring angle is zero or $\pi/2$. Zhou et al. verified this scaling property numerically by solving the equations derived by spherical harmonic expansion [37].

Our numerical results are presented in Figs. 7–9. Fig. 7 shows the profile of shear, density, order parameter and director angle at $N = 5$, $\varepsilon = 0.05$, $De = 0.01$, $\theta_b = 0$. As a result of the boundary potential, there are two waves near the two boundaries in the shear, density and order parameter profiles and the order parameter near the two boundary surfaces is bigger than that in the bulk region. Fig. 8 shows the results when the anchoring angle is $\theta_b = \pi/2$. Normal anchoring introduces two wave troughs in the configuration of the shear, density and order parameter. Our results confirm the scaling property found by Forest et al., except for two boundary layers when $\theta_b = 0$; see Fig. 9. Besides this, we found the density ρ has the same scaling property as the order parameter, and the shear rate is not constant when the De number tends to zero, which is also a boundary potential effect. When

ε decreases, the range of $u_y - 1$ decreases simultaneously. Our numerical results did not get the similar scaling property when normal anchoring is imposed; see Fig. 10.

4.2. Pressure-driven plane Poiseuille flow

In pressure-driven plane Poiseuille flow, we studied the microstructure by varying De and ε. When ε is small enough, for example $\varepsilon = 0.02$, increasing De step by step, the microstructure takes several modes: when De is very small, the flow mode is an elastic-driven steady state similar to the IE state in plane Couette flow; at larger De number, a beautiful branch pattern in director spatial–temporal configuration arises, see Fig. 11. The branches and defects at the crosspoint happened because of the spatial variation of the tumbling rate, which is mainly determined by the local shear rate. Near the two boundary surfaces, the shear rate is biggest, so the tumbling rate is biggest, i.e. the tumbling period is small, which leads to small branches. In the inner region close to the center of the flow region, the shear rate is very small, which leads to a thick root; at larger De number, a wagging region and then a flow-aligning region will arise near the boundary, as the inner region changes little. Finally when the De number is big enough, the flow-aligning mode occupy the entire flow region. But the flow-aligning angle is not uniform, see Fig. 12.

The feedback of the macrostructure of LCPs to the flow velocity field is demonstrated in Fig. 13. In general, tumbling will decrease the average velocity (tumbling region is much larger at
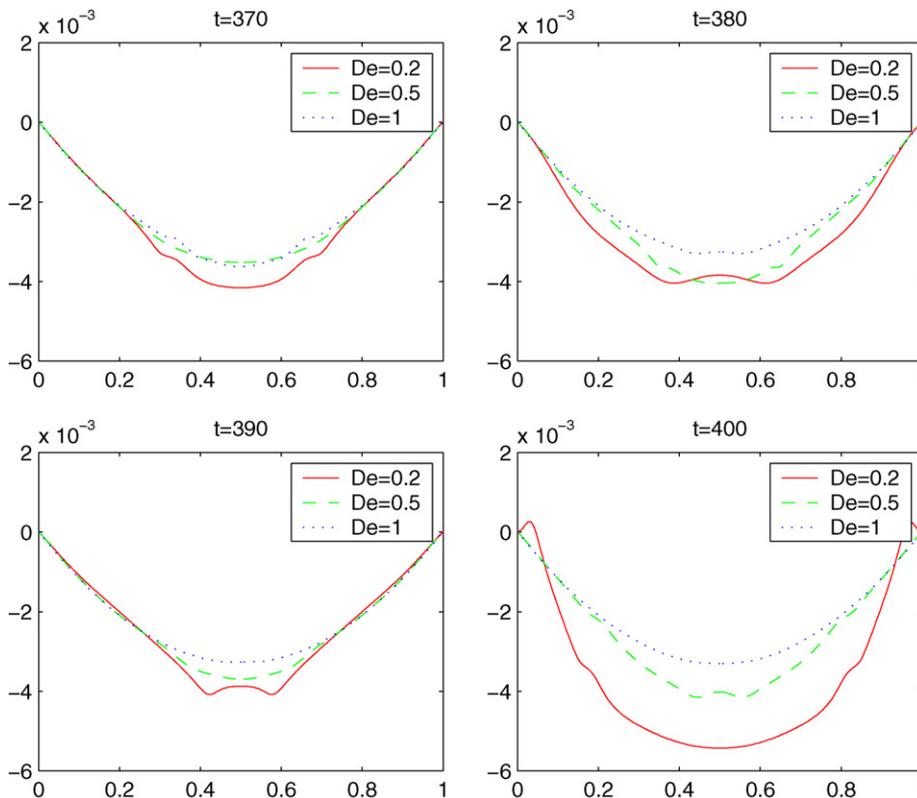

Fig. 13. The difference between the velocity field of the LCP solution and that of the Newtonian fluid at dimensionless time $t = 370, 380, 390, 400$. Note that in the last figure ($t = 400$), there are two intervals near the boundaries in line $De = 0.2$ where the velocity of the LCP solution is bigger than the velocity of the Newtonian fluid.

$De = 0.2$ than at $De = 0.5$ and $De = 1$), but defects will increase the velocity. Note that at $t = 400$, near the two boundaries the velocity of the LCP solution is bigger than the velocity of Newtonian, because of two strong defects near the two boundaries.

The flow depends heavily on N also. When N increases, the tumbling rate increases, tumbling region of the parameter De is bigger, so more defects and branches will arise.

5. Concluding remarks

We presented a new kinetic–hydrodynamic coupled model for the dilute LCP solution for inhomogeneous flow, which accounts for translational diffusion and density variation. It is very easy to extend this model to a concentrated solution.

We applied the coupled kinetic–hydrodynamic model to plane shear flow by restricting the molecular orientation in the shear plane and obtained some significant properties:

- The microstructure is mainly determined by ε, De and N. In plane Couette flow, seven flow modes are predicted by varying ε and De (in some closed models the Ericksen number has a relation with ε and N: $Er = 8/N\varepsilon^2$, but in the molecular kinetic model a simple relation does not exist).
- The multilayer structure of defects is arrested.
- The thickness of the boundary layer is proportional to molecular length l, and also bears somewhat on N, De. The thickness of boundary layer will increase as N increases.
- The tumbling period is proportional to the inverse of shear rate.
- The flow-aligning angle tends to zero as De approaches infinity.
- The scaling properties we obtained in plane Couette flow with tangential anchoring is similar to that predicted by Zhou et al. [37]. Furthermore, our results show that density variation has the same scale De^2 with scalar order parameter.

Similar work in Couette flow was done by Forest et al. [13,37] They used Doi kinetic theory with Marrucci–Greco potential, and neglected translational diffusion. Their numerical approach was based on spherical harmonic expansion. Because of the absence of translational diffusion, that approach cannot predict density variation. The most important difference between numerical results in this paper and theirs is their results did not predict inner defects. We have made sure it is the translational diffusion that introduces inner defects by comparing numerical results with and without translational diffusion. Another difference is we use a boundary potential to ensure boundary molecules anchoring at a certain direction. The boundary potential has an effect on some physical quantities, such as scalar order parameter and density, see Fig. 9. We do not know whether the effects are physical or artificial, until the full three dimensional orientational simulation is performed.

The in-plane restriction of the LCP molecules make the orientation can be represented by an angle. This can cut off the computing effort. But this restriction precludes rog rolling, kayaking and other important and interesting phases. And in three dimensional solution of LCPs, some of the in-plane solu-

tions is unstable with respect to the spatial gradient of orientation. Indeed, our results predict in-plane tumbling instability at low shear rates. And with increasing shear rate, there is a twist instability predicted by Zuniga and Leslie [38], followed by a roll-cell instability [5,6,19]. These all out-of-plane instabilities and its consequences, such as band and strip texture reported by Larson and Mead [21,22], cannot be predicted by any in-plane orientational simulation. However, the in-plane simulation confirm our kinetic–hydrodynamic coupled model with translational diffusion and non-local intermolecular potential. Full three dimensional orientation results will be presented in our later paper.

Acknowledgements

References

[1] M. Doi, S.F. Edwards, The Theory of Polymer Dynamics, Oxford University Press, Oxford, 1986.
[2] Z. Cui, G. Forest, Q. Wang, On weak plane Couette and Poiseuille flows of rigid rod and platelet ensembles, SIAM J. Appl. Math. 66 (4) (2006) 1227–1260.
[3] M. Doi, T. Shimada, K. Okano, Concentration fluctuation of stiff polymers. II. Dynamical structure factor of rod-like polymers in the isotropic phase, J. Chem. Phys. 88 (6) (1988) 4070–4075.
[4] J. Feng, L.G. Leal, Pressure-driven channel flows of a model liquid-crystalline polymer, Phys. Fluids 11 (1999) 2821–2835.
[5] J.J. Feng, J. Tao, L.G. Leal, Roll cells and disclinations in sheared nematic polymers, J. Fluid Mech. 449 (2001) 179.
[6] J. Tao, J.J. Feng, Effects of elastic anisotropy on the flow and orientation of sheared nematic liquid crystals, J. Rheol. 47 (4) (2003) 1051.
[7] J.J. Feng, G. Sgalari, G. Leal, A theory for flowing nematic polymers with orientational distortion, J. Rheol. 44 (5) (2000) 1085.
[8] G. Forest, Q. Wang, R. Zhou, The flow-phase diagram of Doi–Hess theory for sheared nematic polymers II: finite share rates, Rheol. Acta 44 (1) (2004) 80.
[9] M.G. Forest, Q. Wang, R. Zhou, Symmetries of the Doi kinetic theory for nematic polymers of finite and infinite aspect ratio: at rest and in linear flows, Phys. Rev. E 66 (3) (2003) P031712.
[10] M.G. Forest, Q. Wang, Monodomain response of finite-aspect-ratio macromolecules in shear and related linear flows, Rheol. Acta 42 (2003) 20–46.
[11] M.G. Forest, Q. Wang, R. Zhou, The weak shear phase diagram for nematic polymers, Rheol. Acta 43 (1) (2004) 17–37.
[12] M.G. Forest, R. Zhou, Q. Wang, Scaling behavior of kinetic orientational distributions for dilute nematic polymers in weak shear, J. Non-Newtonian Fluid Mech. 116 (2004) 183–204.
[13] M.G. Forest, R. Zhou, Q. Wang, Kinetic structure simulations of nematic polymers in plane Couette cells. II: in-plane structure transitions, Multiscale Model. Simul. 4 (4) (2005) 1280–1304.
[14] M.G. Forest, Q. Wang, H. Zhou, R. Zhou, Structure scaling properties of confined nematic polymers in plane Couette cells: the weak flow limit, J. Rheol. 48 (1) (2004) 175–192.
[15] P.G. de Gennes, J. Prost, The Physics of Liquid Crystals, second ed., Oxford Science Publications, 1993.
[16] G.L. Hand, A theory of anisotropic fluids, J. Fluid Mech. 13 (1962) 33–46.
[17] R. Kupferman, M.N. Kawaguchi, M.M. Denn, Emergence of structure in a model of liquid crystalline polymers with elastic coupling, J. Non-Newtonian Fluid Mech. 91 (2000) 255–271.

[18] R.G. Larson, Arrested tumbling in shearing flows of liquid-crystal polymers, Macromolecules 23 (1990) 3983–3992.

[19] R.G. Larson, Roll-cell instabilities in shearing flows of nematic polymers, J. Rheol. 37 (2) (1993) 175.

[20] R.G. Larson, H.C. Öttinger, Effect of molecular elasticity on out-of-plane orientations in shearing flows of liquid-crystalline polymers, Macromolecules 24 (1991) 6270–6282.

[21] R.G. Larson, D.W. Mead, Development of orientation and texture during shearing of liquid-crystalline polymers, Liq. Cryst. 12 (1992) 75–768.

[22] R.G. Larson, D.W. Mead, The Erickson number and Deborah number cascades in sheared polymeric nematics, Liq. Cryst. 15 (1993) 151–169.

[23] F.M. Leslie, Theory of flow phenomena in liquid crystals, Adv. Liq. Cryst. 4 (1979) 1–81.

[24] G. Marrucci, P.L. Maffettone, Description of the liquid crystalline phase of rodlike polymers at high shear rates, Macromolecules 22 (1989) 4076–4082.

[25] G. Marrucci, F. Greco, The elastic constants of Maier–Saupe rodlike molecule nematics, Mol. Cryst. Liq. Cryst. 206 (1991) 17–30.

[26] G. Marrucci, F. Greco, A molecular approach to the polydomain structure of LCPs in weak shear flows, J. Non-Newtonian Fluid Mech. 44 (1992) 1–13.

[27] G. Marrucci, F. Greco, Flow behavior of liquid crystalline polymers, Adv. Chem. Phys. LXXXVI (1993) 331–405.

[28] A.D. Rey, T. Tsuji, Orientation mode selection mechanisms for sheared nematic liquid crystalline materials, Phys. Rev. E 57 (5) (1998) 5610–5625.

[29] A.D. Rey, T. Tsuji, Recent advances in theoretical liquid crystal rheology, Macromol. Theory Simul. 7 (1998) 623–639.

[30] G. Sgalari, G.L. Leal, J.J. Feng, The shear flow behavior of LCPs based on a generalized Doi model with distortional elasticity, J. Non-Newtonian Fluid Mech. 102 (2002) 361–382.

[31] G. Sgalari, L.G. Leal, E. Meiburg, Texture evolution of sheared liquid crystalline polymers: numerical predictions of roll cells instability, director turbulence, and striped texture with a molecular model, J. Rheol. 47 (6) (2003) 1417–1444.

[32] J.K. Suen, R. Nayak, R.C. Armstrong, R.A. Brown, A wavelet-Galerkin method for simulating the Doi model with orientation-dependent rotational diffusivity, J. Non-Newtonian Fluid Mech. 114 (2003) 197–228.

[34] Q. Wang, E. Weinan, C. Liu, P. Zhang, Kinetic theory for flows of nonhomogeneous rodlike liquid crystalline polymers with a nonlocal intermolecular potential, Phys. Rev. E 65 (2002) 051504.

[35] Q. Wang, A hydrodynamic theory for solutions of nonhomogeneous nematic liquid crystalline polymers of different configurations, J. Chem. Phys. 116 (20) (2002) 9120–9136.

[36] Q. Wang, M.G. Forest, R. Zhou, A kinetic theory for solutions of nonhomogeneous nematic liquid crystalline polymers with density variations, J. Fluids Eng. 126 (2004) 180.

[37] R. Zhou, M.G. Forest, Q. Wang, Kinetic structure simulations of nematic polymers in plane couette cells. I: the algorithm and benchmarks, Multiscale Model. Simul. 3 (4) (2005) 853–870.

[38] I. Zuniga, F.M. Leslie, Shear-flow instabilities in non-flow-aligning nematic liquid crystals, Liq. Cryst. 5 (1989) 725–734.